

# Three-Dimensional Passive-Source Anisotropic Reverse Time Migration for Imaging Lithospheric Discontinuities: The Method

Peng Zou<sup>1</sup> and Jiubing Cheng<sup>1</sup>

<sup>1</sup>State Key Laboratory of Marine Geology, Tongji University

November 21, 2022

## Abstract

The scattered teleseismic body waves have been used intensively to characterize the receiver-side lithospheric structures. The routinely used ray-theory-based methods have their own limitations to image complex structures and tackle strong heterogeneities. The newly developed wave-equation based, passive-source reverse time migration (RTM) approach can overcome such limitations. To date, passive-source RTM has been developed only for isotropic media. However, at least to the first-order, most lithospheric structures possess effective transverse isotropy with spatially variable symmetry direction. It is important to know how if we image the lithospheric discontinuities when seismic anisotropy is treated in an incorrect way. In this paper, we investigate the influence of elastic anisotropy on teleseismic P-to-S conversion at the lithospheric discontinuities and gain insights to explain why an isotropic RTM may fail to focus the converted wavefields from the perspective of relative arrival time variations with backazimuth and shear wave splitting. Accordingly, we extend the passive-source RTM approach for imaging three-dimensional (3-D) lithospheric targets possessing transverse isotropy from the following two aspects: First, the teleseismic recordings with direct P and converted S phases are reverse-time extrapolated using rotated staggered grid (RSG) pseudo-spectral method which can tackle strong heterogeneity and transverse isotropies with symmetry axes in arbitrary direction; Second, the backward elastic wavefields are efficiently decomposed into vector anisotropic P and S modes to support accurate imaging. Two synthetic tests with hierarchical complexities reveal the significance of appropriate treatment of seismic anisotropy in passive-source RTM to characterize the receiver-side fine-scale lithospheric structures.

1 **Three-Dimensional Passive-Source Anisotropic Reverse Time**  
2 **Migration for Imaging Lithospheric Discontinuities: The**  
3 **Method**

4 **Peng Zou<sup>1</sup> and Jiubing Cheng<sup>1</sup>**

5 <sup>1</sup>State Key Laboratory of Marine Geology, Tongji University, Shanghai, China.

6 **Key Points:**

- 7 • Seismic anisotropy in the receiver-side lithosphere has great impact on the scattered,  
8 teleseismic phases.
- 9 • Passive-source anisotropic reverse time migration can tackle strong heterogeneities and  
10 typical anisotropies.
- 11 • The symptoms of the split Ps phases in post-migration backazimuth domain reveal sig-  
12 nificance of appropriate treatments of the anisotropy.

---

Corresponding author: Jiubing Cheng, [cjb1206@tongji.edu.cn](mailto:cjb1206@tongji.edu.cn)

## Abstract

The scattered teleseismic body waves have been used intensively to characterize the receiver-side lithospheric structures. The routinely used ray-theory-based methods have their own limitations to image complex structures and tackle strong heterogeneities. The newly developed wave-equation based, passive-source reverse time migration (RTM) approach can overcome such limitations, provided that multi-component seismograms have been recorded by regionally extensive seismic arrays of reasonable spatial sampling. To date, passive-source RTM has been developed only for isotropic media. However, at least to the first-order, most crustal and upper-mantle structures possess effective transverse isotropy with spatially variable symmetry direction. It is important to know how if we image the lithospheric discontinuities when seismic anisotropy is treated in an incorrect way. In this paper, we investigate the influence of elastic anisotropy on teleseismic P-to-S conversion at the lithospheric discontinuities and gain insights to explain why an isotropic RTM may fail to focus the converted wavefields from the perspective of relative arrival time variations with backazimuth and shear wave splitting. Accordingly, we extend the passive-source RTM approach for imaging three dimensional (3-D) lithospheric targets possessing transverse isotropy from the following two aspects: First, the teleseismic recordings with direct P and converted S phases are reverse-time extrapolated using rotated staggered grid (RSG) pseudo-spectral method which can tackle strong heterogeneity and transverse isotropies with symmetry axes in arbitrary direction; Second, the backward elastic wavefields are efficiently decomposed into vector anisotropic P and S modes to support accurate imaging. Two synthetic tests with hierarchical complexities reveal the significance of appropriate treatment of seismic anisotropy in passive-source RTM to characterize the receiver-side fine-scale lithospheric structures.

## 1 Introduction

In past decades, teleseismic body-wave scattering has been extensively used to characterize discontinuities in earth's crust, lithosphere-asthenosphere boundary, and mantle transition zone. The method commonly used has been the one of receiver functions (RFs), which were introduced and developed by Vinnik (1977) and Langston (1979). In this framework, essentially, the converted S-wave recording is deconvolved with the corresponding direct P-wave recording at each available station assuming a planarly layered earth model. Since then, various refinements have been developed for arrays of receivers. Common conversion point (CCP) stacking techniques are now routinely applied in the RF workflow to image interfaces in the

45 crust and mantle beneath the stations, e.g., Dueker & Sheehan (1997); L. Zhu (2000); Gao &  
46 Liu (2014). Stacking of multiple RFs over finite lateral and depth dimensions is necessary to  
47 enhance the signals of the converted waves as individual RFs often have low signal-to-noise  
48 ratios. Due to this spatial averaging, the CCP method can only produce good results for smoothly  
49 varying structures, and prevents accurate imaging of geologically complex structures, such as  
50 dipping and laterally discontinuous interfaces (e.g., strong interface topography, steep faults,  
51 steps in Moho). Moreover, stacking data from individual stations cannot adequately suppress  
52 scattering or diffraction hyperbola artefacts (L. Chen et al., 2005; Rondenay, 2009).

53 Several techniques have been presented to overcome the limitations of the conventional  
54 RF method. Ryberg & Weber (2000) demonstrated the application of Kirchoff poststack depth  
55 migration to synthetic data, and advocated that the concept of RF migration is theoretically  
56 sound. Revenaugh (1995), Levander et al. (2005), and C. Cheng et al. (2016) developed Kir-  
57 choff prestack depth migration to image scatters and velocity discontinuities. Bostock & Ron-  
58 denay (1999) developed an inverse scattering approach for direct imaging of broadband array  
59 data using the theory developed by Beylkin (1985) for seismic reflection applications, which  
60 exploits an analogy between high-frequency, single scattering and the Radon transform. Pop-  
61 peliers & Pavlis (2003) transformed the teleseismic recordings into ray-parameter and back-  
62 azimuth domain plane waves and migrated them separately. L. Chen et al. (2005) presented  
63 a wave-equation migration method, which back-propagates the CCP stacked RFs with an one-  
64 way phase screen propagator. Referring to a comprehensive theory of reverse-time migration  
65 (RTM) based inverse scattering in elastic media (Brytik et al., 2012), Shang et al. (2012) de-  
66 veloped an elastic RTM approach to image crustal and mantle structures using teleseismic con-  
67 verted waves densely recorded by an array. Unlike the conventional RTM in exploration seis-  
68 mology (Baysal et al., 1983), which involves both source-side and receiver-side wavefields,  
69 this passive-source RTM approach requires only receiver-side backward propagated wavefield  
70 to form an image. Therefore, source related uncertainties, such as in epicenter location and  
71 origin time, are eliminated in teleseismic imaging of the structures beneath stations. By com-  
72 paring the CCP and passive-source RTM results for a synthetic model with an offset in the  
73 Moho structure, Shang et al. (2012) demonstrated the advantages of this wave equation-based  
74 RF migration technique for complex structures. Compared to Kirchhoff migration, RTM is com-  
75 putationally more expensive, but has advantages to account for finite-frequency effects and over-  
76 comes, for example, multipathing in the propagating wavefield. Recently, Li et al. (2018) ex-  
77 tended the passive-source RTM approach to 3-D spherical coordinate system, which may suit

78 for regional and global problems better. Note that all above studies focus on isotropic media,  
79 which limits their application to the lithospheric targets with evident seismic anisotropy, such  
80 as in subduction zone (Huang et al., 2011; Long & Wirth, 2013), orogenic belt(Xie et al., 2017)  
81 and beneath the cratons (Fouch & Rondenay, 2006).

82 Elastic anisotropy is the dependence of wave velocity on propagation direction. Gen-  
83 erally, either orthorhombic or hexagonal symmetry is assumed when analyzing the earth. In  
84 most practice, people examine seismic anisotropy by analyzing variations of body-wave or surface-  
85 wave velocity in two orthogonal directions . The simplest model to explain these variations  
86 of velocity is hexagonal anisotropy or transverse isotropy (TI), although this probably aver-  
87 age variations in other directions (Anderson & Regan, 1983; Savage, 1999). For instance, S-  
88 wave anisotropy of up to 4% is ubiquitous in the upper 200km of the lithosphere (Kaneshima  
89 et al., 1988; Savage, 1999). Anisotropy in the crust can be mainly caused by thin-bedded lay-  
90 ering Backus (1962) and fluid-filled cracks (Crampin, 1984). In some areas (e.g. Tibet, Rus-  
91 sian Urals, New Zealand), the lower crustal anisotropy may range up to 15%, mainly caused  
92 by highly anisotropic schists (Levin & Park, 1997). Upper mantle anisotropy is believed to  
93 result from strain-induced, preferred orientation of mantle minerals (mainly olivine). The sources  
94 to cause S-wave anisotropy also generate P-wave anisotropy with 5 – 9% magnitude in the  
95 subducted slab and the largest crustal anisotropy (14%) related to schist (Eberhart-Phillips &  
96 Reyners, 2009; J. Wang & Zhao, 2012). Another important indicator of seismic anisotropy is  
97 shear wave splitting (SWS), in which the S-wave splits into two orthogonally polarized modes,  
98 each traveling with potentially different velocities (Christensen, 1966). To keep matters sim-  
99 ple but capture the first-order features, seismologists usually explain the direction-dependence  
100 of P- and S-wave velocities and the behavior of shear wave splitting in terms of hexagonal anisotropy  
101 or TI, with vertical, horizontal or tilted symmetry axis (Anderson & Regan, 1983; Thomsen,  
102 1986; Savage, 1999).

103 The passive-source RTM method use both direct P and converted S waves recorded by  
104 an array of stations to image the elastic discontinuities in the lithosphere. Its success relies on  
105 two key elements: an accurate reverse-time propagation of the elastic wavefields, and an imag-  
106 ing condition that can mitigate crosstalks among the wave modes and appropriately tackle shear  
107 wave splitting. It is important to know how if we use an isotropic migration algorithm while  
108 the subsurface medium is anisotropic. In this paper, apart from reviewing elastic body-wave  
109 propagation and polarization, we investigate the influence of elastic anisotropy on the teleseis-  
110 mic converted Ps phases, from the view of relative arrival time and shear wave splitting. Ac-

111 cordingly, we propose an anisotropic RTM method for imaging 3-D lithospheric targets. To  
 112 tackle the hexagonal symmetries not aligned with the computational grids, we choose a ro-  
 113 tated staggered-grid (RSG) pseudo-spectral scheme (Zou & Cheng, 2018) to reconstruct the  
 114 subsurface elastic wavefields. High-fidelity and efficient wave mode decomposition (J. Cheng  
 115 & Fomel, 2014) is used to precondition the reconstructed wavefields for accurately image the  
 116 lithospheric discontinuities. Then, we show two synthetic examples to demonstrate the pro-  
 117 posed approach in crustal extension and subduction zones. Finally, we discuss the ways to pro-  
 118 vide anisotropic velocity models and the possible alternative algorithms to reduce the com-  
 119 putational cost for anisotropic RTM of teleseismic data.

## 120 **2 Teleseismic Body-Waves in Anisotropic Lithosphere**

### 121 **2.1 Elastic body-wave propagation and polarization**

122 For a linear elastic medium, the 3-D time-domain elastodynamic equation with source  
 123 term is given by

$$\rho \partial_t u_i = \partial_j \tau_{ij} + f_i, \quad i = 1, 2, 3, \quad (1)$$

124 where  $\rho = \rho(\mathbf{x})$  denotes density,  $u_i = u_i(\mathbf{x}, t)$  are the particle velocities at a point  $\mathbf{x}$  and  
 125 time  $t$ ,  $\tau_{ij} = \tau_{ij}(\mathbf{x}, t)$  are the stress components and  $f_i = f_i(\mathbf{x}, t)$  are the body-force com-  
 126 ponents. We have used the Einstein summation convention over repeated indices, and a con-  
 127 tracted notation for partial derivatives:  $\partial_t \equiv \partial/\partial t$ , and  $\partial_j \equiv \partial/\partial x_j$ . The stress and particle  
 128 velocity components are related by the 3-D generalized Hooke’s law through the stiffness ten-  
 129 sor  $c_{ijkl}$  as follows:

$$\partial_t \tau_{ij} = c_{ijkl} \partial_l u_j. \quad (2)$$

130 Due to the inherent symmetries of stress and strain and the existence of a unique strain en-  
 131 ergy potential, only 21 elastic stiffness coefficients are independent, which usually simplified  
 132 by Voigt notation (Auld, 1973) as  $c_{ij}$  (here,  $i, j = 1, 2, 3, 4, 5, 6; j \geq i$ ). The principal axes  
 133 (called crystal axes in crystallography) are intrinsic axes, that define the symmetry of the medium.  
 134 Most of the geological systems at different scales can be enough described by monoclinic, or-  
 135 thorhombic, hexagonal and isotropic media, which require 12, 9, 5, and 2 independent elas-  
 136 ticity constants to fully describe the stress-strain relationship in the principal coordinate sys-  
 137 tem, respectively.

138 Seismic waves are described by the elastodynamic equation with P- and S-waves intrin-  
 139 sically coupled. An anisotropic medium “splits” the S-wave into two modes with different ve-

140 locities. In the far-field, the polarization (or particle motion) vectors of the P-wave and the two  
 141 S-waves are orthogonal, but in general not coincident with the dynamic axes defined by the  
 142 propagation vector and plane of constant phase, thus we have the nomenclature of quasi-P (qP)  
 143 and quasi-S (qS) waves. Substituting a plane-wave solution and the generalized Hooke's law  
 144 into equation 1, neglecting the source term, gives the Christoffel equation:

$$(\tilde{\mathbf{G}} - \rho V_m^2 \mathbf{I}) \mathbf{a}_m = 0, \quad (3)$$

145 where  $\tilde{\mathbf{G}}$  represents the Christoffel tensor in the Voigt notation with  $\tilde{G}_{ij} = c_{ijkl} n_j n_l$ , and  
 146  $n_j$  and  $n_l$  are the components of normalized propagation vector in the  $j$ - and  $l$ -th directions,  
 147 with  $i, j, k, l = 1, 2, 3$ . The parameters  $V_m$  ( $m = \text{qP}, \text{qS}_1, \text{qS}_2$ ), which associate with the three  
 148 eigenvalues of Christoffel equation, represent phase velocities of qP, qS<sub>1</sub> (fast qS), qS<sub>2</sub> (slow  
 149 qS) waves, respectively. The corresponding eigenvector  $\mathbf{a}_m$  represents polarization direction  
 150 of the given mode. If an eigenvalue coincides with one of the two remaining eigenvalues, the  
 151 corresponding eigenvector cannot be uniquely determined. We then speak of the degenerate  
 152 case. In realistic cases, the P-wave eigenvalue is well separated from the S-wave eigenvalues.  
 153 This means that the degenerate case does not exist for P-waves. For S waves, however, there  
 154 are two different degenerate cases (Crampin & Yedlin, 1981): (a) In anisotropic media, the two  
 155 eigenvalues coincide locally along certain lines or at certain points on the slowness surface.  
 156 We then speak of S-wave singularities and note that the polarization direction becomes a dis-  
 157 continuous function of phase direction. (b) In isotropic media, the two eigenvalues of S-wave  
 158 coincide globally, and the polarization vectors can be in any two orthogonal transverse direc-  
 159 tion. In both these degenerate cases, the two S modes are coupled, locally or globally, and prop-  
 160 agate as a single wave.

## 161 **2.2 Hexagonal anisotropy in lithosphere**

162 Although various mechanisms will lead to seismic anisotropy in the crust and upper man-  
 163 tle on a handful of scenarios, in many instances the effective anisotropy displays axis (i.e., hexag-  
 164 onal) symmetry to the first order (e.g. Thomsen, 1986; Savage, 1999). It can be caused by in-  
 165 trinsic anisotropy of the dominant mineral (e.g., mica, clay, serpentinite) or by periodic lay-  
 166 ering of materials with different elastic properties (Backus, 1962). Upper mantle anisotropy  
 167 is most likely due to lattice preferred orientation (LPO) of olivine-rich rocks under disloca-  
 168 tion creep (Mainprice et al., 2005). Foliated rocks such as gneisses and schists which believed  
 169 to be the main cause of seismic anisotropy in the upper crust are orthorhombic or lower in sym-  
 170 metry. However, compilations of laboratory measurements of many laminated or foliated rocks

171 by Christensen (1966) and Godfrey et al. (2000) reveal that orthogonal measurements within  
 172 the planes of foliation are similar (less than a few percent) particularly when compared with  
 173 the measurement normal to the planes (several to > 10 percent). In these cases the approx-  
 174 imation of hexagonal symmetry is valid.

175 Hexagonal symmetry requires five elastic constants in addition to the direction of the sym-  
 176 metry axis, and it is also called transverse isotropy (TI). When the symmetry axis is vertical,  
 177 such anisotropy is called radial anisotropy or TI with a vertical symmetry axis (VTI). To sep-  
 178 arate the influence of the anisotropy from the ‘isotropic’ quantities chosen as the qP and qS  
 179 velocities along the symmetry axis, Thomsen (1986) presented an alternative parameterization  
 180 for VTI media:

$$v_{p0} = \sqrt{\frac{c_{33}}{\rho}}, \quad (4a)$$

$$v_{s0} = \sqrt{\frac{c_{44}}{\rho}}, \quad (4b)$$

$$\epsilon = \frac{c_{11} - c_{33}}{2c_{33}}, \quad (4c)$$

$$\delta = \frac{(c_{13} + c_{44})^2 - (c_{33} - c_{44})^2}{2c_{33}(c_{33} - c_{44})}, \quad (4d)$$

$$\gamma = \frac{c_{66} - c_{44}}{2c_{44}}, \quad (4e)$$

181 where  $v_{p0}$  and  $v_{s0}$  are the qP- and qS-wave velocities, respectively, along the symmetry axis.  
 182 The parameter  $\epsilon$  is controlled by the fractional difference between the vertical ( $\sqrt{c_{33}/\rho}$ ) and  
 183 horizontal ( $\sqrt{c_{11}/\rho}$ ) P-wave velocities and is therefore analogous to the traditional measure  
 184 of velocity anisotropy (Crampin, 1989). The parameter  $\gamma$  is an SH-wave version of  $\epsilon$ . Although  
 185 the definition of  $\delta$  is less transparent than  $\epsilon$  and  $\gamma$ , this parameter is responsible for the an-  
 186 gular dependence of P and SV wave velocities, especially in the phase directions very close  
 187 to the symmetry axis. We call  $\epsilon$  as P-wave anisotropy,  $\gamma$  as S-wave anisotropy and  $\delta$  as ellip-  
 188 ticity (Becker et al., 2006). A useful advantage of this notation is that the dimensionless pa-  
 189 rameters,  $\epsilon$ ,  $\delta$  and  $\gamma$ , collapse to zero in the case of isotropy. In general, two angles (dip an-  
 190 gles  $\alpha$  and strike angle  $\phi$ ) are required to specify an orientation of the symmetric axis, and the  
 191 stiffness tensor in the Cartesian coordinate can be obtained through the Bond transformation  
 192 from the principal coordinate frame. For the TI with a horizontal symmetry axis (HTI), Tsvankin  
 193 (1997) introduced Thomsen parameters of the “equivalent” VTI model, which can be used to  
 194 express the phase velocities and carry out seismic imaging.

### 195 **2.3 The influence of anisotropy on teleseismic Ps phases**

196 The analysis of scattered, teleseismic body waves to characterize the receiver-side litho-  
 197 sphere is now among the most widely used means of resolving fine-scale structure in these  
 198 outer layers of the Earth. The lower mantle is generally assumed a smoothly varying and ra-  
 199 dial velocity structure. Therefore, the teleseismic wave propagation is relatively simple and  
 200 can be effectively modeled by plane-wave sources over the breadth of the array. As the inci-  
 201 dent wavefield encounters discontinuities of elastic properties in the upper mantle and crust,  
 202 it first generates forward scattered and converted waves that follow the incident waves to the  
 203 surface. Then, the free-surface produces P and S reflections that further interact with under-  
 204 lying structure to produce backscattered energy recorded by the receiver array. Crustal rever-  
 205 berations are often considered a source of noise in lithospheric studies using the direct P and  
 206 P-to-S conversions. Real data from epicentral distances less than  $30^\circ$  are complicated by trip-  
 207 lications caused by upper mantle discontinuities, and data from epicentral distances larger than  
 208  $90^\circ$  are complicated by interaction with the core-mantle boundary. For passive-source RTM,  
 209 we will focus on the forward P-to-S scatterings in the lithosphere associated with the tele-  
 210 seismic P-wave at epicentral distance of  $30^\circ < \Delta < 90^\circ$ . In the isotropic case, an incom-  
 211 ing plane P wave generates a single Ps phase at the discontinuity, whereas in the anisotropic  
 212 case the converted S-wave generally splits into two orthogonally polarized modes, each trav-  
 213 eling with different phase velocities and directions (Figure 1).

214 Ps receiver functions in hexagonal anisotropy media exhibit distinct azimuthal patterns,  
 215 both on radial and transverse components. For instance, one can observe azimuthal amplitude  
 216 variations on the radial component, polarity change on the transverse component and undu-  
 217 lation of the delay time between direct P and converted Ps phases (Levin & Park, 1998). The  
 218 time lag between the fast and slow modes of the split Ps phases is a quantitative indicator com-  
 219 monly used to constrain S-wave crustal anisotropy (e.g., McNamara & Owens, 1993; Liu &  
 220 Niu, 2012).

221 For the RTM of teleseismic Ps phases, the key is applying an imaging condition to the  
 222 decomposed P and S modes of the backward propagated elastic wavefields (Shang et al., 2012).  
 223 In isotropic media, the divergence and curl operators are the traditional method for P/S sep-  
 224 aration. One can construct two-dimensional (2-D) anisotropic wave mode separation opera-  
 225 tors analogous to divergence and curl, based on the qP-qS polarization orthogonality (Dellinger,  
 226 1991). Fundamental complications occur with this method in three dimensions for shear waves,

227 because it is geometrically impossible to define a single global shear mode without discon-  
 228 tinuities in polarization. Even weak orthorhombic anisotropy can cause the qS modes to split  
 229 apart in a surprising way and the qS<sub>1</sub> and qS<sub>2</sub> modes are not individually continuous. This  
 230 problem is not insurmountable; the isotropic separation into P, SV and SH waves enjoys wide  
 231 use despite the discontinuity for vertically propagating S-waves. Similar separations are use-  
 232 ful for TI media, because the qS-waves can be designated as qSV and qSH modes with glob-  
 233 ally continuous polarizations, except in the degenerate direction along the symmetry axis (Dellinger,  
 234 1991; Yan & Sava, 2009). The SH-wave always polarizes in the isotropy plane as a pure mode  
 235 and the qSV-wave always polarizes in the plane formed by the symmetry axis and the prop-  
 236 agation direction. Therefore, in this study, the influence of seismic anisotropy on RTM of the  
 237 Ps phases will be investigated from the view of relative arrival times between the direct qP  
 238 phase and the converted qSV and qSH phases. For simplicity, we will not strictly distinguish  
 239 the nomenclature P, SV and SH with qP, qSV and qSH in the following sections.

240 A hexagonal medium has a single axis of rotational symmetry. Therefore, all seismic  
 241 signatures depend just on phase angle, i.e., the angle between the symmetry axis and prop-  
 242 agation direction. In the weak-anisotropy approximation, Thomsen (1986) derived a linearized  
 243 formulation of the phase velocities for the three wave modes:

$$v_p(\theta) = v_{p0}(1 + \delta \sin^2 \theta \cos^2 \theta + \epsilon \sin^4 \theta), \quad (5a)$$

$$v_{sv}(\theta) = v_{s0} \left[ 1 + \frac{v_{p0}^2}{v_{s0}^2} (\epsilon - \delta) \sin^2 \theta \cos^2 \theta \right], \quad (5b)$$

$$v_{sh}(\theta) = v_{s0}(1 + \gamma \sin^2 \theta), \quad (5c)$$

244 where  $\theta$  is the phase angle. Accordingly, we can evaluate the influence of hexagonal anisotropy  
 245 on the propagation and imaging of the teleseismic data. For a given planar P-wave incidence  
 246 with horizontal slowness  $p$  and backazimuth  $\Phi$ , the relative arrival times of the converted qSV  
 247 and qSH phases associated with a lithospheric interface at the depth of  $H$  below a homoge-  
 248 neous and anisotropic layer (Figure 1b) can be respectively expressed as:

$$T_{p-sv}(p, \Phi) = H \left[ \sqrt{\frac{1}{v_{sv}^2(\theta_{sv}(p, \Phi))} - p^2} - \sqrt{\frac{1}{v_p^2(\theta_p(p, \Phi))} - p^2} \right], \quad (6)$$

249 and

$$T_{p-sh}(p, \Phi) = H \left[ \sqrt{\frac{1}{v_{sh}^2(\theta_{sh}(p, \Phi))} - p^2} - \sqrt{\frac{1}{v_p^2(\theta_p(p, \Phi))} - p^2} \right], \quad (7)$$

250 with  $\theta_p$ ,  $\theta_{sv}$  and  $\theta_{sh}$  representing phase angles of the transmitted qP, qSV and qSH waves, re-  
 251 spectively. Given the medium parameters and the incident direction defined by  $p$  and  $\Phi$ , one  
 252 can calculate the phase angles using the Snell's law.

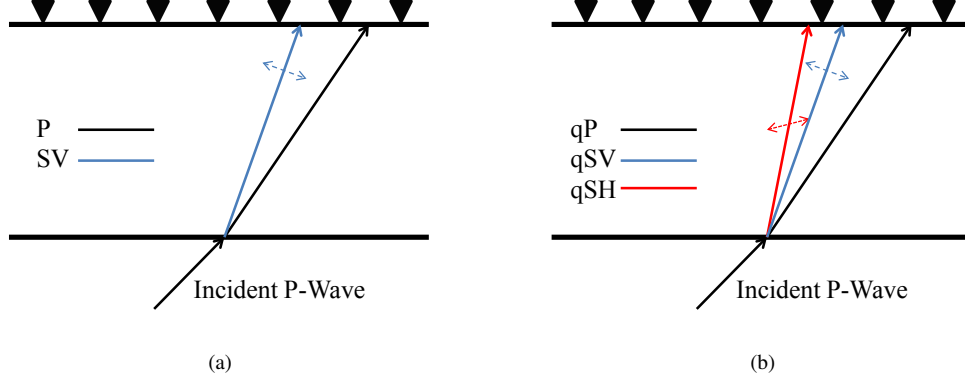


Figure 1: A schematic diagram illustrating raypaths of teleseismic body-waves in the localized zone below the array. A planar P-wave from a distant earthquake travels through an isotropic layer (a) or a transversely isotropic layer (b) before being recorded by the stations (black triangles). The solid lines denote wave propagation direction of each wave mode, and the thin dash lines indicate polarization directions of S-waves. In the presence of anisotropy, the converted Ps wave splits into two orthogonally polarized modes, which can be designated as qSV and qSH waves in the process of wavefield propagation.

253 We illustrate the relative arrival times of the Ps phases on a crustal extension model, in  
 254 which the depth of Moho is  $33\text{km}$  and the crustal anisotropy results from predominately gran-  
 255 ite with fluid-filled cracks, e.g., Jones et al. (1999). The stiffness tensor was calculated assum-  
 256 ing an isotropic granitic host rock with P-wave velocity of  $6.5\text{km/s}$ , S-wave velocity of  $3.8\text{km/s}$   
 257 and a density of  $2.6\text{g/cm}^3$ . The effects of vertical fluid-filled cracks were modelled using the  
 258 self-consistent scheme (SCM) (Nishizawa, 1982). Cracks in the crust have an aspect ratio of  
 259 0.06 and the host rock has a crack porosity of 5 percent (resulting in a crack density of 20  
 260 percent). The coefficients of crack orientation distribution function (CODF) were chosen so  
 261 that the crustal layer possesses HTI symmetry, of which the Thomsen parameters of the equiv-  
 262 alent VTI model is given by  $\epsilon = -0.08$ ,  $\gamma = -0.06$  and  $\delta = -0.16$ . In addition, the elas-  
 263 ticity of the isotropic mantle material is defined with P-wave velocity of  $7.8\text{km/s}$ , S-wave ve-  
 264 locity of  $4.6\text{km/s}$  and a density of  $3.0\text{g/cm}^3$ , respectively. Figure 2 displays variations of the  
 265 relative arrival times for qP-qSV, qP-qSH phases and an isotropic converted phase for refer-

266 ence. We observe that both  $T_{p-sv}$  and  $T_{p-sh}$  vary with backazimuth, and the former has greater  
 267 variations. In this example, the largest deviation from the isotropic counterpart approaches  $0.5s$ ,  
 268 which means a depth shift of about  $5.0km$  if neglecting the anisotropy.

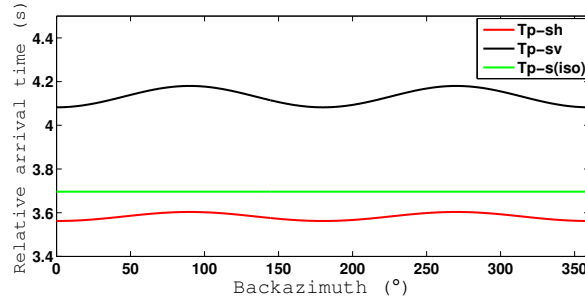


Figure 2: The relative arrival times of qP-qSV, qP-qSH and their isotropic counterpart associated with backazimuth of an incident planar P-wave with a horizontal slowness of  $0.053s/km$  in a crustal extension model.

269 We further check the waveforms of the converted Ps phases in the synthetic three-component  
 270 (3C) seismograms for the crustal extension model. As shown in Figure 3a, a regular station  
 271 network is deployed on the surface of the model, of which the size is  $80km \times 80km \times 60km$   
 272 in three dimension. Plane-wave sources with horizontal slowness between  $0.040s/km$  and  $0.077s/km$   
 273 are used to mimic the teleseismic sources at  $30^\circ \sim 90^\circ$  epicentral distance. We record 3C  
 274 particle velocity with the stations in a recording time of  $20s$ . These synthetic seismograms will  
 275 be used as "data" for the first RTM experiment in the example section. Figure 3b shows a 3C  
 276 seismogram recorded by one of the station for a planar P-wave incidence. We can observe the  
 277 split Ps phases on the two horizontal components, of which the x-component is dominated by  
 278 the P-to-SV conversion and the y-component dominated by the P-to-SH conversion, with a time  
 279 lag of about  $0.5s$ . This essentially agrees with the analytic estimate of their kinematics using  
 280 the phase velocity formulations (Figure 2).

### 281 **3 passive-source Reverse Time Migration in Anisotropic Lithosphere**

282 Deployments of regionally extensive seismic arrays of reasonable spatial sampling yield  
 283 teleseismic data amenable to array-based processing (e.g., RTM) for delineating receiver-side  
 284 small-scale heterogeneities in the crust and upper mantle. In general, passive-source RTM mainly  
 285 consists of three steps (Shang et al., 2012; Li et al., 2018): First, back-propagated elastic wave-  
 286 fields in subsurface are reconstructed through reverse-time extrapolating the multi-component

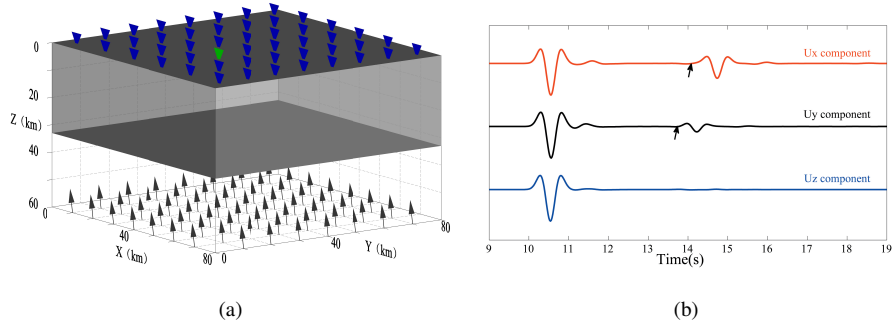


Figure 3: Synthetic teleseismic recordings on the 3-D crustal extension model: (a) Sketch map of the station network (denoted by triangles) and the model geometry beneath the recording network. (b) 3C seismograms recorded by a station (denoted by green triangle) for a planar P-wave incidence with a backazimuth of  $135^\circ$  (due north) and incidence angle of  $25^\circ$  (from the vertical). The relative arrival times of the converted S phases are picked on  $x$ - and  $y$ -components of the seismograms.

287 seismograms. Then, P/S separation of the elastic wavefields is carried out at each time-step  
 288 to mitigate crosstalks between the two wave modes. Finally, an appropriate imaging condi-  
 289 tion is applied to the decoupled P and S fields to yield an image of the elastic discontinuity.  
 290 Stacking amounts of images of the selected earthquakes improves the quality of final result.  
 291 In this procedure, both wavefield extrapolation and mode decomposition can be affected by  
 292 P- and S-wave anisotropies in the crust and upper mantle. In the subduction zone, orogenic  
 293 belt or near the periphery of the craton, depth-dependent tilted hexagonally symmetry is very  
 294 common (Long & Wirth, 2013; Xie et al., 2017). To adapt anisotropic symmetries in the litho-  
 295 sphere not aligned with the computational grids, we will first review a pseudo-spectral method  
 296 that can simulate elastic wave propagation in 3-D arbitrary anisotropic media. Then we will  
 297 present a vector-product imaging condition based on an efficient mode decomposition of the  
 298 elastic wavefields in heterogeneous TI media with the polarization projection.

### 299 3.1 Pseudo-spectral method for anisotropic wavefield extrapolation

300 Among the most popular numerical methods for simulating seismic wave propagation,  
 301 we choose pseudo-spectral method (PSM) using rotated staggered grids (RSG) (Zou & Cheng,  
 302 2018) as a solver of the first-order elastic wave equations in 3-D anisotropic media due to the  
 303 three factors: First, the PSM can save computational memory and time because the spectral

304 operators permit larger grid spacing to calculate the spatial derivatives (Kosloff & Baysal, 1982).  
 305 Second, when the symmetry axis of a TI medium is not aligned with the computational grid,  
 306 a straightforward use of the standard staggered grids (SSG) is problematic because of essen-  
 307 tially different and complicated representations of Hooke’s law. The RSG configuration makes  
 308 the PSM applicable to 3-D arbitrary anisotropic media and at the same time avoids any cum-  
 309 bersome interpolation operation such as in the SSG implementation (Zou & Cheng, 2018), be-  
 310 cause three particle velocity components with all the stiffness coefficients are defined at the  
 311 same location and all stress components are placed at the center of the grid cells (Saenger &  
 312 Bohlen, 2004). Third, the particle velocity components calculated by the RSG-based PSM can  
 313 be directly used for wave mode decomposition because all of them are defined at the same nodes  
 314 and thus don’t require any adjustments as in the SSG-based schemes, e.g., Zhang & McMechan  
 315 (2010).

316 Grid staggering is essential for a PSM to suppress the non-causal ringing artifacts in sim-  
 317 ulating seismic wave propagation, but the standard implementation can only be used to model  
 318 anisotropy up to orthorhombic media and the symmetry axis aligned with the computational  
 319 grid. In RSG-based PSM, the spatial derivatives in equations (1) and (2) can be calculated by  
 320 the following discrete formula:

$$D_j^\pm \varphi = \sum_{k_j=0}^{k_j(N)} ik_j \cdot s^\pm \cdot \tilde{\varphi}(k_j) e^{ik_j j}, \quad (8)$$

321 with

$$s^\pm = e^{\pm i(k_x \Delta x/2 + k_y \Delta y/2 + k_z \Delta z/2)}, \quad (9)$$

322 in which  $k_j$  ( $j = x, y, z$ ) denotes the wavenumber with respect to one of the coordinates, and  
 323  $k_j(N)$  represents the corresponding Nyquist wavenumber,  $s^+$  or  $s^-$  is a forward or backward  
 324 phase shift to amend the staggered differential operator,  $i$  is an imaginary unit,  $\tilde{\varphi}$  denotes the  
 325 Fourier transform of  $\varphi$ . With these spectral derivative operators, the elastodynamic equation  
 326 and stress-strain equation can be solved by using

$$\rho \partial_t u_i = D_j^+ \tau_{ij} + f_i, \quad (10)$$

327 and

$$\partial_t \tau_{ij} = c_{ijkl} D_l^- u_k. \quad (11)$$

328 The equation of motion only involves forward-shifted spectral derivative operators, whereas  
 329 the constitutive relation only involves backward-shifted spectral derivative operators. This im-  
 330 plies that all the phase shifts can be merged into the spectral derivative operations, and thus  
 331 no extra fast Fourier transformation is required. This RSG-based PSM provides a good solu-

332 tion for simulating 3-D elastic wave propagation in a TI medium with strong heterogeneities  
 333 and arbitrary variations in the direction of the symmetry axis. More details can be found in  
 334 Zou & Cheng (2018).

### 335 **3.2 Imaging based on wave mode vector decomposition**

336 In elastic RTM, for whether active- or passive-source seismic data, decoupling the wave  
 337 modes in the far-field is a prerequisite for imaging to get physically interpretable results with  
 338 fewer crosstalks (Shang et al., 2012; C. Wang et al., 2016). In general, for the well-behaved  
 339 qP mode, the wave polarization  $\mathbf{a}_p$  can be determined by solving the Christoffel equation (3).  
 340 Therefore, Dellinger (1991) proposed an approach to separate qP and non-qP (qS) fields based  
 341 on polarization projection only involving the polarization direction of qP-wave ( $\mathbf{a}_p$ ). However,  
 342 the polarization directions of the two qS modes cannot be consistently determined in this way  
 343 because of the S-wave singularities (Crampin & Yedlin, 1981). So it is not wise to separate  
 344  $qS_1$  and  $qS_2$  in the extrapolated wavefields for the imaging purpose. To our interest, in TI me-  
 345 dia, the qS-waves can be designated as qSV and qSH modes with globally continuous polar-  
 346 izations, except in the degenerate direction along the symmetry axis. The far-field qP, qSV and  
 347 qSH waves in the same propagation direction possess polarization orthogonality, which pro-  
 348 vides theoretical cornerstone to decouple them in the plane-wave domain during wavefield ex-  
 349 trapolation. Accordingly, Yan & Sava (2009) suggested to further decouple the qS field into  
 350 qSV and qSH modes based on the qP-qSV-qSH polarization orthogonality in TI media. To honor  
 351 vector fidelity, the far-field elastic wavefield at any moment can be decomposed through (Zhang  
 352 & McMechan, 2010):

$$\mathbf{U}_m(\mathbf{k}) = \bar{\mathbf{a}}_m(\mathbf{k})[\bar{\mathbf{a}}_m(\mathbf{k}) \cdot \mathbf{U}(\mathbf{k})], \quad (12)$$

353 where  $\bar{\mathbf{a}}_m$  ( $m = qP, qSV, qSH$ ) represents the normalized polarization vector in the phase  
 354 direction  $\mathbf{k}$ , and  $\mathbf{U}$  is the vector wavefield of particle velocity in wavenumber-domain. This  
 355 mode decomposition preserves the original physical units, phases, particle motion amplitudes  
 356 and directions. To tackle spatial heterogeneities of the anisotropic media, the equation (12) can  
 357 be extended to a generalized Fourier integral operator (J. Cheng & Fomel, 2014):

$$\mathbf{u}_m(\mathbf{x}) = \int e^{i\mathbf{k}\cdot\mathbf{x}} \bar{\mathbf{a}}_m(\mathbf{x}, \mathbf{k})[\bar{\mathbf{a}}_m(\mathbf{x}, \mathbf{k}) \cdot \mathbf{U}(\mathbf{k})]d\mathbf{k}. \quad (13)$$

358 In passive-source RTM, separation of qP and qS fields is sufficient for the imaging condition  
 359 to characterize the lithospheric discontinuities. In this case, equation 13 is only used for iso-  
 360 lating qP vector field, and the qS vector fields can be directly obtained, i.e.,  $\mathbf{u}_{qS}(\mathbf{x}) = \mathbf{u}(\mathbf{x}) -$   
 361  $\mathbf{u}_{qP}(\mathbf{x})$ . Further separation of qSV and qSH modes is helpful for investigating the effects of

362 anisotropy (e.g., S-wave splitting and azimuthal signatures) on the RTM images. For TI me-  
 363 dia with spatial heterogeneities, the above integral operator is equivalent to a nonstationary fil-  
 364 tering. The computation complexity of the straight-forward implementation is  $O(N^2)$ , which  
 365 is prohibitively expensive when the size of model  $N$  is large. We apply a model-adaptive low-  
 366 rank approximation to the mixed-domain integral kernels in equation 13 (J. Cheng & Fomel,  
 367 2014) to reduce the computation complexity to  $O(rN \log N)$ , and the rank  $r$  is very small and  
 368 usually below the order of tens.

369 To take full advantage of the vector information (e.g. polarization and polarity) of the  
 370 separated qP and qS wavefields, we prefer to applying the imaging condition proposed by C. Wang  
 371 et al. (2016) in exploration seismology to the RTM of teleseismic data. Thus the vectorial cross-  
 372 correlation of the separated wavefields

$$I_{ps}(\mathbf{x}) = \sum_{n=1}^{n_s} \frac{w_n}{|\kappa_n|} \int_0^T [\mathbf{u}_{qP}(\mathbf{x}, t) \cdot \mathbf{u}_{qS}(\mathbf{x}, t)]_n dt, \quad (14)$$

373 is used to image the elastic discontinuities that cause the qP-to-qS mode conversion for  $n_s$  se-  
 374 lected earthquakes within the required epicentral distance. The scale factor

$$\kappa_n = \int_0^T [\bar{\mathbf{a}}_p(\mathbf{x}, t) \cdot \bar{\mathbf{a}}_s(\mathbf{x}, t)]_n dt, \quad (15)$$

375 is applied to balance the image amplitudes, and the weight  $w_n$  can be determined according  
 376 to the image quality of an individual event (such as signal-to-noise ratio). We can obtain two  
 377 more images by vectorial cross-correlation of the separated qP and qSV (or qP and qSH) fields  
 378 for interpretive use. Note that, this vector imaging condition automatically avoids the polarity-  
 379 reversal issue that often damages the elastic RTM based on conventional imaging condition,  
 380 and maintains a consistent polarity for a given elastic contrast (C. Wang et al., 2016).

381 3-D RTM is a computationally heavy task and the cost is generally proportional to the  
 382 number of earthquakes used in imaging. For passive-source RTM in isotropic media, Li et al.  
 383 (2018) adopted a parallel algorithm on high-performance cluster of multi-core CPUs. The com-  
 384 putational demands tremendously increase in 3-D anisotropic media because more partial deriva-  
 385 tives related to none-zero stiffness coefficients are required to extrapolate the wavefields. For  
 386 TI media with strong spatial heterogeneities, it still takes a large amount of time to decom-  
 387 pose the elastic wavefields into pure mode fields, even though the low-rank approximate al-  
 388 gorithm has been used. To make the proposed 3-D anisotropic RTM computationally afford-  
 389 able, our solution is to leverage the massively parallel architecture of graphic processing units  
 390 (GPUs) to accelerate the computation in wavefield extrapolation and mode decomposition.

## 4 Numerical Examples

In this section, we will test the approach and investigate how anisotropy influences the RTM results of the lithospheric discontinuities with two synthetic data sets. We first explore how the image of the Moho may be biased if seismic data acquired over a transversely isotropic crustal layer are imaged with inaccurate Thomsen parameters or assuming isotropy. Then we investigate what gains can be made by passive-source anisotropic RTM in the subduction zone possessing realistic transverse isotropies with varied symmetry axes in different layers. These numerical experiments are implemented on a workstation with four NVIDIA RTX 2080 Ti GPU cards.

### 4.1 Crustal extension model

We first study the effects of crustal anisotropy and consider a single HTI layer overlying an isotropic elastic half-space. The 3D-3C seismograms synthesized by using the RSG-based PSM in the previous section are processed with the passive-source RTM algorithm. For the 120 events, the incident angles at the Moho vary from  $15^\circ$  to  $25^\circ$  in  $2^\circ$  increments, while the back-azimuths vary from  $0^\circ$  to  $360^\circ$  in  $15^\circ$  increments. For simplicity, we employ Ricker wavelet with central frequency of  $1.0Hz$  as the source time function. This simplification is justifiable as a source-equalization and deconvolution step can be applied to real teleseismic data to remove the source effects, e.g., Rondenay (2009). In order to investigate the influence of anisotropy, we respectively carry out four experiments with: (a) the true anisotropic model; (b) an inaccurate anisotropic model by setting  $\epsilon = 0$ ; (c) an inaccurate anisotropic model by setting  $\gamma = 0$ ; (d) an isotropic model by setting  $\epsilon = 0$ ,  $\gamma = 0$  and  $\delta = 0$ . We do not check the impact of  $\delta$  because it only influences the wave propagation around the symmetry axis of the HTI layer and thus has few effect on the teleseismic phases to our interests in this experiment.

Both wavefield extrapolation and P/S mode decomposition are based on the given migration velocity models. Figure 4 displays the RTM images and common image gathers (CIGs) in the backazimuth domain with these models. We observe that correct imaging depth and high signal-to-noise ratio can only be guaranteed with the true anisotropic model. Remarkable residual moveouts varied with the backazimuths lead to inaccurate RTM images and artifacts resulting from mode crosstalks and unfocused wavefields, when the inaccurate migration velocity models are used. To further explain the imaging results, we decompose the S wavefields

422 into SV and SH modes, and output the CIGs of the P-SV and P-SH converted phases. Along  
423 with the time-to-depth conversion according to equations (6 and 7), these CIGs provide insight-  
424 ful clues to reveal the influence of the anisotropic parameters (Figures 4 and 5). Energy gaps  
425 on the P-SV and P-SH CIGs are clearly observed because there are no P-to-SV (or P-to-SH)  
426 conversion when the elastic waves propagate perpendicular to (or parallel with) the symme-  
427 try axis of the HTI media. These CIGs indicate patterns of amplitude variations with the back-  
428 azimuths for P-SV and P-SH phases. Weak P-to-SH conversion at this interface causes rel-  
429 atively small amplitudes on the P-SH CIGs. Neglecting the P-wave anisotropy by setting  $\epsilon =$   
430  $0$ , P-SV and P-SH CIGs display almost consistent residual moveouts in the backazimuth do-  
431 main, and eventually lead to about  $5km$  misfit between the stacked image of the Moho and  
432 its true depth, see Figures 4c, 5d, 5e and 5f. As shown in the last two rows in Figure 4, ne-  
433 glecting the S-wave anisotropy leads to severely distorted images for the Moho in the backaz-  
434 imuth domain, and two split interfaces in the stacked images. For the corresponding P-SV and  
435 P-SH CIGs in Figure 5, we see that accurate P-wave anisotropy guarantees correct imaging  
436 depths for the P-SV conversion at various backazimuths, whereas inappropriate treatments of  
437 S-wave anisotropy result in back-propagation of the split S-wave fields with incorrect phase  
438 velocities and severe mode leakage in the P-SH images at most backazimuths. As shown in Fig-  
439 ures 5g and 5i, the P-SH conversions nearly all are imaged at shallower depths for various back-  
440 azimuths. When we use an isotropic velocity model by setting  $\epsilon$ ,  $\gamma$  and  $\delta$  as zeros, the P-SV  
441 conversions all focused at much deeper locations while the P-SH conversions are focused at  
442 slightly shallower locations for various backazimuths. In this case, the depth errors of the P-  
443 SH images are relatively small because the phase velocities of P and SH modes have simi-  
444 lar changing trends when assuming isotropy (equation 5). For the split images of the Moho  
445 in Figures 5i and 5l, the upper flattened events are the contribution of P-SV conversions while  
446 the lower bending events mainly result from the leaked P-SV energy due to inappropriate treat-  
447 ments of S-wave splitting. The NVIDIA RTX 2080 Ti GPU has a large amount of computa-  
448 tional units but limited memory resource (only 12GB per card), so we need to use RSG-based  
449 PSM for allowing large grid spacing for 3-D wavefield extrapolation. Thanks to the power-  
450 ful computational capability, it takes half an hour to finish the RTM task of all 120 earthquakes  
451 with four these GPU cards.

## 4.2 Subduction model

Then we demonstrate the passive-source anisotropic RTM approach with a synthetic teleseismic data on a subduction model, which is summarized and simplified from the Hikurangi subduction zone (Eberhart-Phillips & Reyners, 2009) and northeast Japan subduction zone (Huang et al., 2011). It contains an isotropic layer in the crust, trench-normal (HTI) anisotropy of 6% and 2% for P- and S-waves in the mantle wedge, and trench-parallel (tilted TI) anisotropy of 8% and 2% for P- and S-waves in the intra subducting slab, respectively. For calculation purposes, we take it as a multi-layer VTI model with the equivalent Thomsen parameters. We assume that there exists no lateral variation along the  $y$  direction and ignore the subslab anisotropy for simplicity. Figure 6a displays the subduction structures with the vertical P-wave velocities in the section perpendicular to the slab, while the vertical S-wave velocities are given by a constant  $V_p/V_s$  ratio. We have synthesized the scattered Ps phases for 24 teleseismic P-wave incidences to illuminate the subduction zone, of which the incidence angles vary from  $15^\circ$  to  $21^\circ$  with an uniform increment of  $3.5^\circ$  and the backazimuths vary from  $5^\circ$  to  $360^\circ$  with an uniform increment of  $30^\circ$ . The anisotropic models are preconditioned through gaussian smoothing with a radius of  $8.0km$  for RTM.

We observe remarkable differences between the RTM results with and without taking into account anisotropy. In the anisotropic RTM image (Figure 6b), the main peaks of the events match well with the elastic discontinuities of the true models and yield good constraints on the subduction structures. Neglecting the anisotropy, the RTM algorithm results in a problematic image for the subducting slab (Figure 6c): First, the top boundary is gradually smeared and eventually split into two events with strong positive polarities, while the bottom boundary is severely smeared and represented by two unfocused events with negative polarities as the mantle wedge becomes thick. Second, the maximum deviation of the slab depths exceed  $5.0km$  beneath the thick anisotropic layers. Third, the signal-to-noise ratio descends due to unfocusing of the back-propagated energy and insufficient P/S mode decoupling when assuming isotropy. The CIGs further reveal that the anisotropic RTM guarantees correct imaging depths for all backazimuths, whereas the isotropic RTM causes wrong imaging depths and fails to focus the split S-wave fields (Figure 7).

## 5 Discussion

The success of the proposed approach to image the 3-D anisotropic lithosphere relies on the following conditions: a dense multicomponent seismic network, high-performance computation, and appropriate anisotropic velocity models. Li et al. (2018) and Jiang et al. (2019) have investigated the spatial sampling requirements on the surface for RTM and pointed out that the distance between two stations should be in the range of 5-10 km for a typical maximum frequency of 1.0 Hz of the teleseismic RFs. The GPU-based wavefield extrapolation and mode decomposition makes passive-source RTM computationally affordable for regional seismological studies. In presence of strong heterogeneity and anisotropy, the polarization-based mode decomposition is still a computational burden even though we have resorted to the low-rank approximation algorithm. A possible approximate solution to avoid separating the P and S fields is to isolate the direct P and its coda and then respectively back-propagate with smooth anisotropic velocity models. A further simplification may be to back-propagate the separated P and Ps phases with pure-mode propagators of qP and qS waves which honor the wavefield kinematics, e.g., J. Cheng & Kang (2014, 2016).

Accurate models of P- and S-wave velocities are essential for RTM of the teleseismic Ps phases to produce reliable structural images. For many years the most widely used 1-D model of the Earth's seismic velocities has been the Preliminary Reference Earth Model (PREM) (Dziewonki & Anderson, 1981). The updated crust and lithosphere models, CRUST1.0 (Laske et al., 2013) and its extension LITHO1.0 (Pasyanos et al., 2014) delineate elastic properties of multi-layer sediment and crust with nominal resolution to  $1^\circ$ , constrained by many different datasets, including extremely large datasets of relatively short-period velocity measurements and compilations of receiver function constraints and active source seismic studies. They provide P- and S-wave velocities for 3-D RTM if the subsurface structures are relatively simple or there is no finer model available in the studied region. The parameters describing P- and S-wave anisotropies and the direction of the symmetry axis are also required to image the lithospheric structures with TI symmetry. Shear wave splitting measurements (e.g., Yuan & Beghein (2013); Rumpker et al. (2014)) and anisotropy-aware RF analyses (e.g., Levin & Park (1997); Eckhardt & Rabbel (2011)) can provide constraints to these parameters of the crust and upper mantle. The rapid growth in global seismic instrumentation, combined with the implementation of automated methods, have enabled the generation of a variety of global, continental-scale anisotropic tomography models, e.g., Lebedev & Hilst (2008); Yuan & Beghein (2013); Chang et al. (2015); Schaeffer et al. (2016) and see Zhao et al. (2016) for a review. With the recent

514 emergence of large-scale dense arrays of broad-band instruments, the mapping of the 3-D dis-  
515 tribution of velocity and anisotropy has been performed with increasingly higher resolution,  
516 for instance using adjoint tomography e.g., M. Chen et al. (2015); H. Zhu et al. (2020), now  
517 approaching the accuracy required for passive-source RTM to improve the lithospheric imag-  
518 ing. Theoretically, full waveform inversion (FWI, Tarantola, 1984) has the potential to dra-  
519 matically improve the resolution of tomographic models due to the exploitation of both the  
520 amplitude and phase of seismic waves. However, the real data application of anisotropic FWI  
521 still an important challenge and needs substantial efforts (Beller & Chevrot, 2020).

## 522 **6 Conclusions**

523 To characterize the fine-scale structures in the anisotropic crust and upper mantle with  
524 the scattered teleseismic data, we have proposed an array-based passive-source 3-D elastic RTM  
525 approach that honors the azimuthal variations of the relative arrival times of the converted Ps  
526 phases and the presence of shear wave splitting. Compared with the isotropic counterpart, it  
527 has the following differences and improvements: First, elastic wavefield backward propaga-  
528 tion using the 3-D RSG-based PSM and polarization-based vector decomposition of qP and  
529 qS fields support accurate imaging in heterogeneous media with vertical, horizontal and tilted  
530 hexagonal symmetries. Second, low-rank approximate polarization projection and GPU-based  
531 acceleration make the 3-D anisotropic RTM algorithm computationally affordable. The numer-  
532 ical test on the simple crustal extension model with HTI symmetry provides useful insights  
533 for the imaged P-to-S (including P-to-SV and P-to-SH) conversions in the stacked and back-  
534 azimuth domains at the lithospheric discontinuities, with or without appropriate treatments of  
535 the seismic anisotropy. The synthetic example on the subduction model with strong hetero-  
536 geneities and spatially varied TI symmetries reveals the necessity to apply passive-source anisotropic  
537 RTM to effectively characterize the boundaries and the shape of the subducted slab. With con-  
538 stantly emerging deployments of regionally extensive seismic arrays and increasing efforts for  
539 3-D regionally anisotropic model building, the proposed wave-equation based approach will  
540 play an important role in 3-D lithospheric imaging.

## 541 **Acknowledgments**

542 This work is supported by the National Natural Science Foundation of China (42074157 &  
543 41674117) and the National Key R&D Program of China (2017YFB0202903). We appreci-  
544 ate Mei Xue and Youqiang Yu for their useful suggestions, and Chenlong Wang for provid-

545 ing the original 2-D passive source RTM code. The first author thanks Tengfei Wang and Si-  
 546 hai Wu for the help in GPU-based parallel computing. All the data is generated by the meth-  
 547 ods presented in the paper which can be easily reproduced with the given model parameters.  
 548 The codes of low rank approximation for wave mode decomposition are available in Mada-  
 549 gascar open-source software package (<http://www.ahay.org>).

## 550 **References**

- 551 Anderson, D. L., & Regan, J. (1983). Uppermantle anisotropy and the oceanic lithosphere.  
 552 *Geophysical Research Letters*, *10*(9), 841–844.
- 553 Auld, B. A. (1973). *Acoustic fields and waves in solids* (Vol. I). Wiley, New York.
- 554 Backus, G. E. (1962). Long-wave elastic anisotropy produced by horizontal layering. *Jour-  
 555 nal of Geophysical Research*, *67*(11), 4427–4440.
- 556 Baysal, E., Kosloff, D. D., & Sherwood, J. W. (1983). Reverse time migration. *Geophysics*,  
 557 *48*(11), 1514–1524.
- 558 Becker, T. W., Chevrot, S., Schulte-Pelkum, V., & Blackman, D. K. (2006). Statistical  
 559 properties of seismic anisotropy predicted by upper mantle geodynamic models. *Journal  
 560 of Geophysical Research: Solid Earth*, *111*(B8).
- 561 Beller, S., & Chevrot, S. (2020). Probing depth and lateral variations of upper-mantle seis-  
 562 mic anisotropy from full-waveform inversion of teleseismic body-waves. *Geophysical  
 563 Journal International*, *222*(1), 352–387.
- 564 Beylkin, G. (1985). Imaging of discontinuities in the inverse scattering problem by inversion  
 565 of a causal generalized radon transform. *Journal of Mathematical Physics*, *26*(1), 99–108.
- 566 Bostock, M., & Rondenay, S. (1999). Migration of scattered teleseismic body waves. *Geo-  
 567 physical journal international*, *137*(3), 732–746.
- 568 Brytik, V., De Hoop, M. V., & Van Der Hilst, R. D. (2012). Elastic-wave inverse scatter-  
 569 ing based on reverse time migration with active and passive source reflection data. *Inverse  
 570 problems and applications: Inside out II*, *60*, 411.
- 571 Chang, S.-J., Ferreira, A. M., Ritsema, J., van Heijst, H. J., & Woodhouse, J. H. (2015).  
 572 Joint inversion for global isotropic and radially anisotropic mantle structure including  
 573 crustal thickness perturbations. *Journal of Geophysical Research: Solid Earth*, *120*(6),  
 574 4278–4300.
- 575 Chen, L., Wen, L., & Zheng, T. (2005). A wave equation migration method for receiver func-  
 576 tion imaging: 1. theory. *Journal of Geophysical Research: Solid Earth*, *110*(B11).

- 577 Chen, M., Niu, F., Liu, Q., Tromp, J., & Zheng, X. (2015). Multiparameter adjoint to-  
578 mography of the crust and upper mantle beneath east asia: 1. model construction and  
579 comparisons. *Journal of Geophysical Research: Solid Earth*, *120*(3), 1762–1786.
- 580 Cheng, C., Bodin, T., & Allen, R. M. (2016). Three-dimensional pre-stack depth migra-  
581 tion of receiver functions with the fast marching method: a kirchhoff approach. *Geophysi-  
582 cal Journal International*, *205*(2), 819–829.
- 583 Cheng, J., & Fomel, S. (2014). Fast algorithms for elastic-wave-mode separation and vector  
584 decomposition using low-rank approximation for anisotropic media. *Geophysics*, *79*(4),  
585 C97–C110.
- 586 Cheng, J., & Kang, W. (2014). Simulating propagation of separated wave modes in general  
587 anisotropic media, part i: qp-wave propagators. *Geophysics*, *79*(1), C1–C18.
- 588 Cheng, J., & Kang, W. (2016). Simulating propagation of separated wave modes in general  
589 anisotropic media, part ii: qs-wave propagators. *Geophysics*, *81*(2), C39–C52.
- 590 Christensen, N. I. (1966). Shear wave velocities in metamorphic rocks at pressures to 10  
591 kilobars. *Journal of Geophysical Research*, *71*(14), 3549–3556.
- 592 Crampin, S. (1984). Effective anisotropic elastic constants for wave propagation through  
593 cracked solids. *Geophysical Journal International*, *76*(1), 135–145.
- 594 Crampin, S. (1989). Suggestions for a consistent terminology for seismic anisotropy. *Geo-  
595 physical Prospecting*, *37*(7), 753–770.
- 596 Crampin, S., & Yedlin, M. (1981). Shear-wave singularities of wave propagation in  
597 anisotropic media. *Journal of Geophysics*, *49*, 43–46.
- 598 Dellinger, J. (1991). *Anisotropic seismic wave propagation*. Ph.D. thesis, Stanford Univer-  
599 sity.
- 600 Dueker, K. G., & Sheehan, A. F. (1997). Mantle discontinuity structure from midpoint  
601 stacks of converted p to s waves across the yellowstone hotspot track. *Journal of Geophys-  
602 ical Research: Solid Earth*, *102*(B4), 8313–8327.
- 603 Dziewonski, A. M., & Anderson, D. L. (1981). Preliminary reference earth model. *Physics  
604 of the Earth and Planetary Interiors*, *25*(4), 297–356.
- 605 Eberhart-Phillips, D., & Reyners, M. (2009). Three-dimensional distribution of seismic  
606 anisotropy in the hikurangi subduction zone beneath the central north island, new zealand.  
607 *Journal of Geophysical Research: Solid Earth*, *114*(B6).
- 608 Eckhardt, C., & Rabbel, W. (2011). Preceiver functions of anisotropic continental crust: a  
609 erarchic catalogue of crustal models and azimuthal waveform patterns. *Geophysical Jour-*

- 610 *nal International*(187), 439-479.
- 611 Fouch, M. J., & Rondenay, S. (2006). Seismic anisotropy beneath stable continental interi-  
612 ors. *Physics of the Earth and Planetary Interiors*, 158(2-4), 292-320.
- 613 Gao, S. S., & Liu, K. H. (2014). Mantle transition zone discontinuities beneath the contigu-  
614 ous united states. *Journal of Geophysical Research: Solid Earth*, 119(8), 6452–6468.
- 615 Godfrey, N. J., Christensen, N. I., & Okaya, D. A. (2000). Anisotropy of schists: Contri-  
616 bution of crustal anisotropy to active source seismic experiments and shear wave splitting  
617 observations. *Journal of Geophysical Research: Solid Earth*, 105(B12), 27991–28007.
- 618 Huang, Z., Zhao, D., & Wang, L. (2011). Seismic heterogeneity and anisotropy of the hon-  
619 shu arc from the japan trench to the japan sea. *Geophysical Journal International*, 184(3),  
620 1428–1444.
- 621 Jiang, X., Zhu, L., Hu, S., & Rong, H. (2019). Three-dimensional reverse-time migration of  
622 teleseismic receiver functions using the phase-shift-plus-interpolation method. *Journal of*  
623 *Geophysical Research: Solid Earth*, 217(1), 1047–1057.
- 624 Jones, K., Warner, M., & Brittan, J. (1999). Anisotropy in multi-offset deep-crustal seismic  
625 experiments. *Geophysical Journal International*, 138(2), 300–318.
- 626 Kaneshima, S., Ando, M., & Kimura, S. (1988). Evidence from shear-wave splitting for the  
627 restriction of seismic anisotropy to the upper crust. *Nature*, 335(6191), 627.
- 628 Kosloff, D., & Baysal, E. (1982). Forward modelling by a Fourier method. *Geophysics*, 47,  
629 1402-1412.
- 630 Langston, C. A. (1979). Structure under mount rainier, washington, inferred from teleseismic  
631 body waves. *Journal of Geophysical Research: Solid Earth*, 84(B9), 4749–4762.
- 632 Laske, G., Masters, G., Ma, Z., & Pasyanos, M. (2013). Update on crust1.0 – a 1-degree  
633 global model of earths crust. *In Geophysical Research Abstracts*, 15.
- 634 Lebedev, S., & Hilst, R. D. V. D. (2008). Global upper-mantle tomography with the au-  
635 tomated multimode inversion of surface and s-wave forms. *Geophysical Journal Interna-*  
636 *tional*, 173, 505-518.
- 637 Levander, A., Niu, F., Symes, W. W., & Nolet, G. (2005). Imaging teleseismic p to s scat-  
638 tered waves using the kirchhoff integral. *Geophysical Monograph-American Geophysical*  
639 *Union*, 157, 149.
- 640 Levin, V., & Park, J. (1997). Crustal anisotropy in the ural mountains foredeep from teleseis-  
641 mic receiver functions. *Geophysical Research Letters*, 24(11), 1283–1286.
- 642 Levin, V., & Park, J. (1998). P-sh conversions in layered media with hexagonally symmetric

- 643 anisotropy: a cookbook. *Pure and Applied Geophysics*, 151, 669–697.
- 644 Li, J., Shen, Y., & Zhang, W. (2018). Three-dimensional passive-source reverse-time mi-  
645 gration of converted waves: The method. *Journal of Geophysical Research: Solid Earth*,  
646 123(2), 1419–1434.
- 647 Liu, H., & Niu, F. (2012). Estimating crustal seismic anisotropy with a joint analysis of  
648 radial and transverse receiver function data. *Geophysical Journal International*, 188(1),  
649 144–164.
- 650 Long, M. D., & Wirth, E. A. (2013). Mantle flow in subduction systems: The mantle wedge  
651 flow field and implications for wedge processes. *Journal of Geophysical Research: Solid  
652 Earth*, 118(2), 583–606.
- 653 Mainprice, D., Tommasi, A., Couvy, H., Cordier, P., & Frost, D. (2005). Pressure sensitivity  
654 of olivine slip systems and seismic anisotropy of earth's upper mantle. *Nature*, 433(7027),  
655 731–3.
- 656 McNamara, D. E., & Owens, T. J. (1993). Azimuthal shear wave velocity anisotropy in  
657 the basin and range province using moho ps converted phases. *Journal of Geophysical Re-  
658 search: Solid Earth*, 98(B7), 12003–12017.
- 659 Nishizawa, O. (1982). Seismic velocity anisotropy in a medium containing oriented cracks.  
660 *Journal of Physics of the Earth*, 30(4), 331–347.
- 661 Pasyanos, M. E., Masters, T. G., Laske, G., & Ma, Z. (2014). Litho1.0: An updated crust and  
662 lithospheric model of the earth. *Journal of Geophysical Research: Solid Earth*, 119(3),  
663 2153–2173.
- 664 Poppeliers, C., & Pavlis, G. L. (2003). Three-dimensional, prestack, plane wave migration  
665 of teleseismic p-to-s converted phases: 1. theory. *Journal of Geophysical Research: Solid  
666 Earth*, 108(B2).
- 667 Revenaugh, J. (1995). A scattered-wave image of subduction beneath the transverse ranges.  
668 *Science*, 268(5219), 1888–1892.
- 669 Rondenay, S. (2009). Upper mantle imaging with array recordings of converted and scattered  
670 teleseismic waves. *Surveys in Geophysics*, 30(4-5), 377–405.
- 671 Rumpker, G., Kaviani, A., & Latifi, K. (2014). Ps-splitting analysis for multilayered  
672 anisotropic media by azimuthal stacking and layer stripping. *Geophysical Journal Inter-  
673 national*(199), 146–163.
- 674 Ryberg, T., & Weber, M. (2000). Receiver function arrays: a reflection seismic approach.  
675 *Geophysical Journal International*, 141(1), 1–11.

- 676 Saenger, E. H., & Bohlen, T. (2004). Finite-difference modeling of viscoelastic and  
677 anisotropic wave propagation using the rotated staggered grid. *Geophysics*, 69(2), 583-  
678 591.
- 679 Savage, M. (1999). Seismic anisotropy and mantle deformation: what have we learned from  
680 shear wave splitting? *Reviews of Geophysics*, 37(1), 65–106.
- 681 Schaeffer, A. J., Lebedev, S., & Becker, T. W. (2016). Azimuthal seismic anisotropy in  
682 the earth's upper mantle and the thickness of tectonic plates. *Geophysical Journal Interna-*  
683 *tional*, 207(8), 901-933.
- 684 Shang, X., de Hoop, M. V., & van der Hilst, R. D. (2012). Beyond receiver functions: Pas-  
685 sive source reverse time migration and inverse scattering of converted waves. *Geophysical*  
686 *Research Letters*, 39(15).
- 687 Tarantola, A. (1984). Inversion of seismic reflection data in the acoustic approximation.  
688 *Geophysics*, 49, 1259-1266.
- 689 Thomsen, L. (1986). Weak elastic anisotropy. *Geophysics*, 51(10), 1954–1966.
- 690 Tsvankin, I. (1997). Reflection moveout and parameter estimation for horizontal transverse  
691 isotropy. *Geophysics*, 62(2), 614–629.
- 692 Vinnik, L. (1977). Detection of waves converted from p to sv in the mantle. *Physics of the*  
693 *Earth and Planetary Interiors*, 15(1), 39–45.
- 694 Wang, C., Cheng, J., & Arntsen, B. (2016). Scalar and vector imaging based on wave mode  
695 decoupling for elastic reverse time migration in isotropic and transversely isotropic media.  
696 *Geophysics*, 81(5), S383–S398.
- 697 Wang, J., & Zhao, D. (2012). P wave anisotropic tomography of the nankai subduction zone  
698 in southwest japan. *Geochemistry, Geophysics, Geosystems*, 13(5).
- 699 Xie, J., Ritzwoller, M. H., Shen, W., & Wang, W. (2017). Crustal anisotropy across east-  
700 ern tibet and surroundings modeled as a depth-dependent tilted hexagonally symmetric  
701 medium. *Geophysical Journal International*, 209(1), 466–491.
- 702 Yan, J., & Sava, P. (2009). Elastic wave-mode separation for VTI media. *Geophysics*, 74(5),  
703 WB19–WB32.
- 704 Yuan, K., & Beghein, C. (2013). Seismic anisotropy changes across upper mantle phase tran-  
705 sitions. *Earth and Planetary Science Letters*, 374, 132-144.
- 706 Zhang, Q., & McMechan, G. A. (2010). 2D and 3D elastic wavefield vector decomposition  
707 in the wavenumber domain for VTI media. *Geophysics*, 75(3), D13-D26.
- 708 Zhao, D., Sheng, Y., & Xin, L. (2016). Seismic anisotropy tomography: New insight into

- 709       subduction dynamics. *Gondwana Research*, 33, 24-43.
- 710       Zhu, H., Stern, R. J., & Yang, J. (2020). Seismic evidence for subduction-induced mantle  
711       flows underneath middle america. *Nature Communications*, 11(1), 1–12.
- 712       Zhu, L. (2000). Crustal structure across the san andreas fault, southern california from tele-  
713       seismic converted waves. *Earth and Planetary Science Letters*, 179(1), 183–190.
- 714       Zou, P., & Cheng, J. (2018). Pseudo-spectral method using rotated staggered grid for elastic  
715       wave propagation in 3d arbitrary anisotropic media. *Geophysical Prospecting*, 66, 47-61.

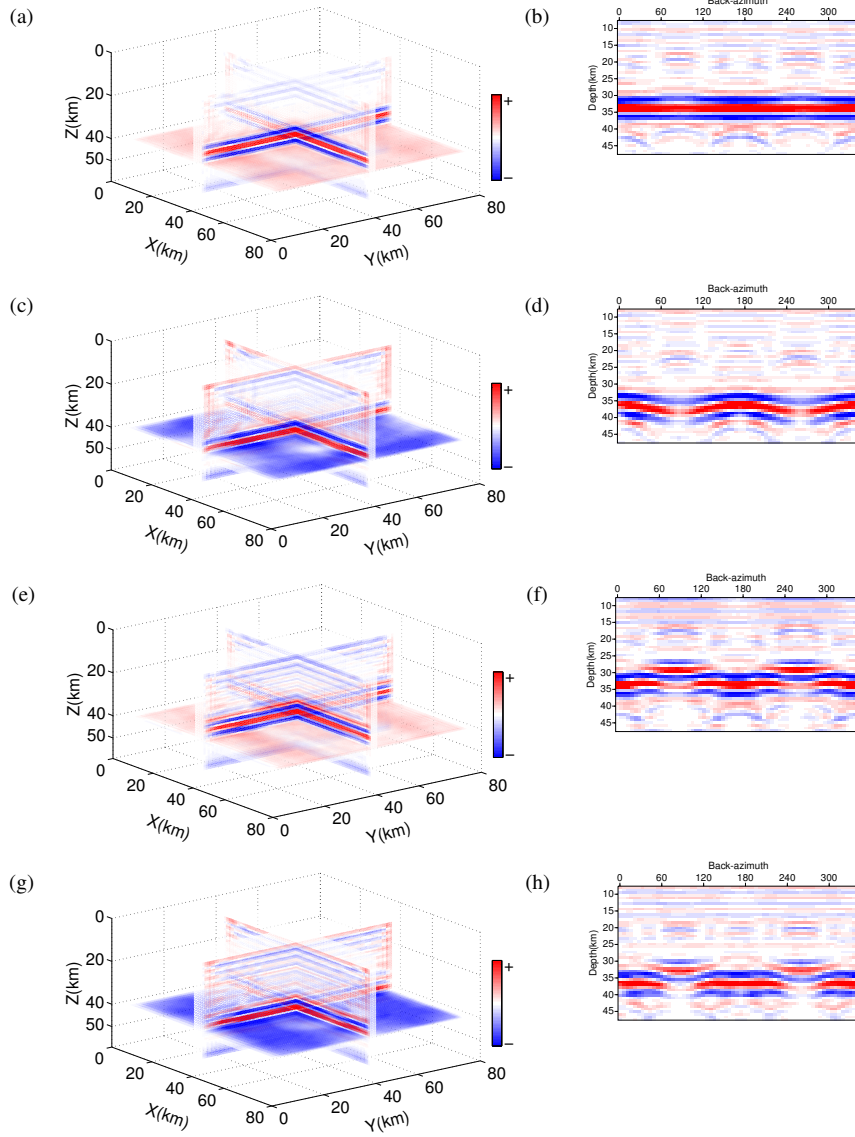


Figure 4: 3-D anisotropic RTM images (left) and common image gathers (right) obtained with (a, b) the true anisotropic model, and inaccurate anisotropic models by setting (c, d)  $\epsilon = 0$ , (e, f)  $\gamma = 0$ , (g, h)  $\epsilon = 0, \gamma = 0$  and  $\delta = 0$ . The true depth of the Moho is  $33\text{km}$  and the horizontal slices in the 3-D RTM images are shown at the depth of  $40\text{km}$ .

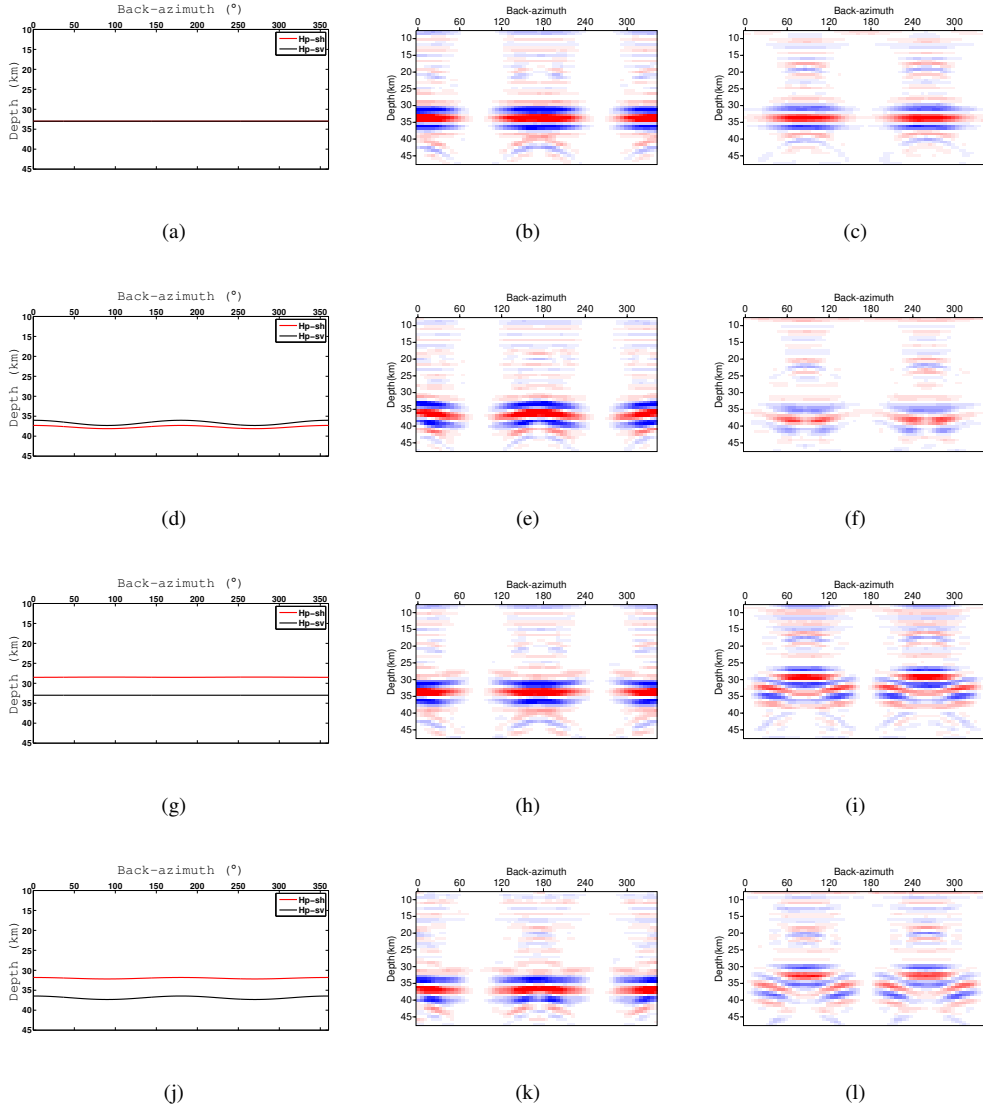
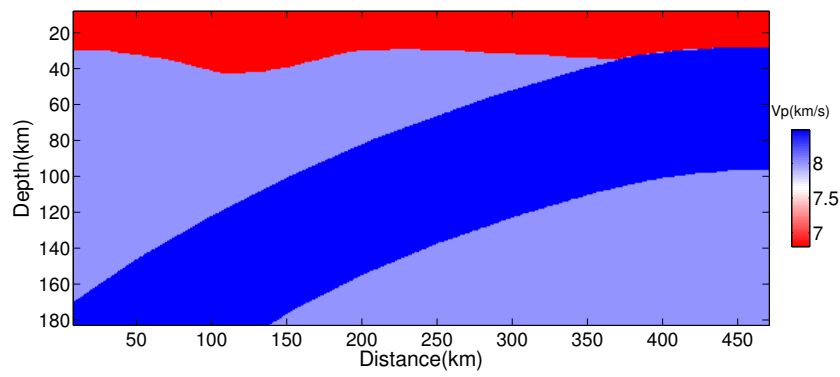
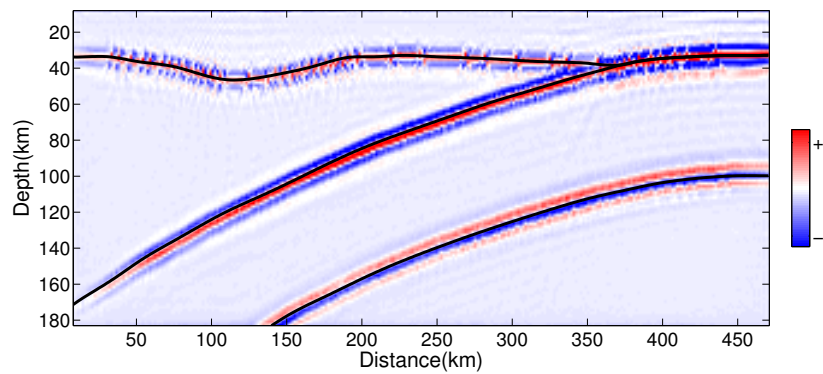


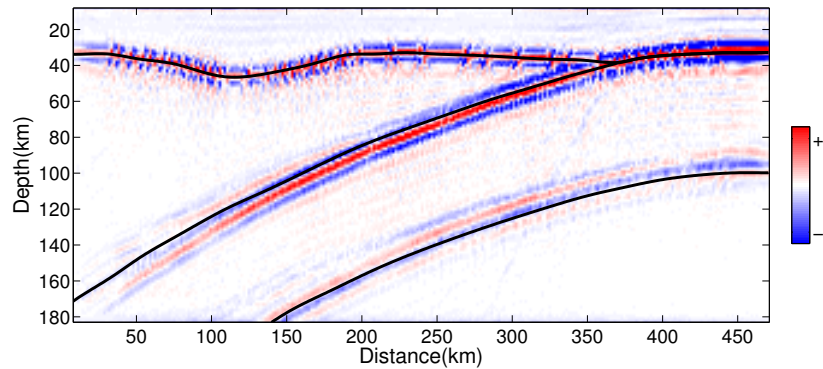
Figure 5: Estimated imaging depths using the phase velocity formulations (left) and the common image gathers for the decoupled P-SV (middle) and P-SH (right) conversions with different migration velocity models: (a, b, c) true anisotropic model; (d, e, f) inaccurate anisotropic model by setting  $\epsilon = 0$ ; (g, h, i) inaccurate anisotropic model by setting  $\gamma = 0$ ; and (j, k, l) isotropic model by setting  $\epsilon = 0, \gamma = 0$  and  $\delta = 0$ .



(a)



(b)



(c)

Figure 6: Image result of one vertical slice perpendicular to the strike of the subduction zone: (a) is the P-wave velocity model of the simplified subduction zone; (b) is the 3-D passive-source RTM image result of the subduction zone structure considering all the anisotropic effects. (c) is the image result ignoring all the anisotropic parameters. The thin black lines in (b) and (c) depict the true elastic discontinuity interfaces.

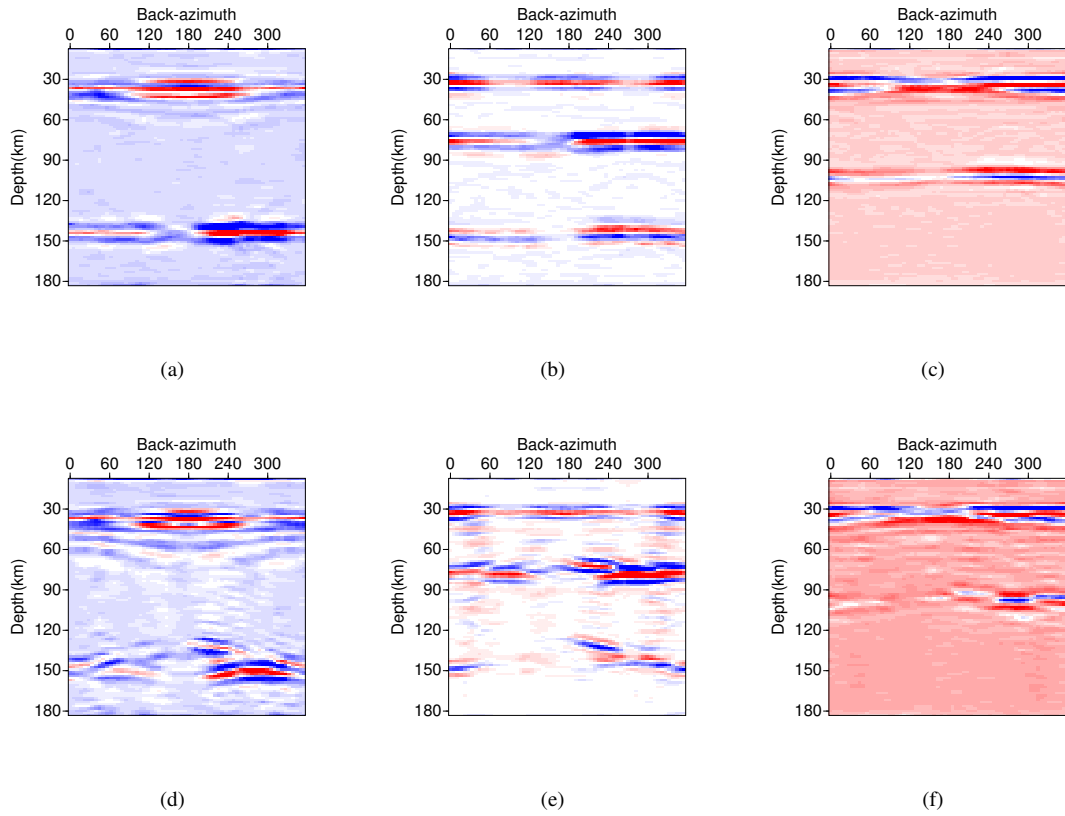


Figure 7: The common image gathers at 72km(a,d), 240km(b,e) and 420km(c,f), respectively. (a, b, c) are the result of 3-D passive-source anisotropic RTM and (d, e, f) are the result of 3-D passive-source isotropic RTM.